MATERIALS SCIENCE

Low-frequency lattice phonons in halide perovskites explain high defect tolerance toward electron-hole recombination

Weibin Chu^{1,2}, Qijing Zheng¹, Oleg V. Prezhdo², Jin Zhao^{1,3,4}*, Wissam A. Saidi⁵*

Low-cost solution-based synthesis of metal halide perovskites (MHPs) invariably introduces defects in the system, which could form Shockley-Read-Hall (SRH) electron-hole recombination centers detrimental to solar conversion efficiency. Here, we investigate the nonradiative recombination processes due to native point defects in methylammonium lead halide (MAPbl₃) perovskites using ab initio nonadiabatic molecular dynamics within surface-hopping framework. Regardless of whether the defects introduce a shallow or deep band state, we find that charge recombination in MAPbl₃ is not enhanced, contrary to predictions from SRH theory. We demonstrate that this strong tolerance against defects, and hence the breakdown of SRH, arises because the photogenerated carriers are only coupled with low-frequency phonons and electron and hole states overlap weakly. Both factors appreciably decrease the nonadiabatic coupling. We argue that the soft nature of the inorganic lattice with small bulk modulus is key for defect tolerance, and hence, the findings are general to other MHPs.

Copyright © 2020
The Authors, some rights reserved; exclusive licensee
American Association for the Advancement of Science. No claim to original U.S. Government Works. Distributed under a Creative
Commons Attribution
NonCommercial
License 4.0 (CC BY-NC).

INTRODUCTION

The metal halide perovskites (MHPs) have enormous potential for optoelectronic applications including solar cells and light-emitting diodes. Several studies have shown that methylammonium lead halide perovskites MAPbX₃ (MA = CH₃NH₃; X = Cl, Br, I), and especially MAPbI₃, have many unique properties, such as high optical absorptions (1, 2), long electron-hole (e-h) diffusion lengths (3, 4), shallow dominant point defects (5-7), and electronically benign grain boundaries (7, 8). Because of intensive research and interest in these materials, we have witnessed, in the past 10 years, a marked increase in the power conversion efficiencies (PCEs) of MHP-based solar cells from 3.5 to 23.3% (9), which is comparable to record efficiencies of commercial thin-film copper indium gallium diselenide and CdTe-based solar cells (10, 11). Nevertheless, the reported PCE is still inferior to the Shockley-Queisser's theoretical limit of 30 to 33% for solar absorbers with band gaps in the 1.2 to 1.6 eV energy range (12, 13). This calls for a better understanding of efficiency losses due to electron-hole recombinations that are predominantly nonradiative (14–16).

The low-cost synthesis of perovskites is one of the main attractive features of these new photo-absorbers. However, because of the relatively soft ionic nature of MHPs, this approach will invariably introduce different intrinsic or extrinsic dopants in the system (17–20). In traditional semiconductors, cation or anion doping can produce defect states in the band gap, which may form *e-h* recombination centers via the Shockley-Read-Hall (SRH) process, and consequently

¹ICQD/Hefei National Laboratory for Physical Sciences at the Microscale, CAS Key Laboratory of Strongly-Coupled Quantum Matter Physics, and Department of Physics, University of Science and Technology of China, Hefei, Anhui 230026, China. ²Departments of Chemistry, and Physics and Astronomy, University of Southern California, Los Angeles, CA 90089, USA. ³Department of Physics and Astronomy, University of Pittsburgh, PA 15260, USA. ⁴Synergetic Innovation Center of Quantum Information and Quantum Physics, University of Science and Technology of China, Hefei, Anhui 230026, China. ⁵Department of Mechanical Engineering and Materials Science, University of Pittsburgh, Pittsburgh, PA 15261, USA.

*Corresponding author. Email: alsaidi@pitt.edu (W.A.S.); zhaojin@ustc.edu.cn (J.Z.)

suppress the solar energy conversion efficiency by converting the photon energy into heat (21). While several theoretical studies concluded that thermodynamically stable intrinsic defects in MAPbI₃ have relatively shallow defect states and hence are electronically benign (1, 6, 7, 22, 23), these conclusions are based on static T = 0 K calculations without accounting for the inelastic electron-phonon interactions. Given that the effective working temperature of a solar cell at room temperature with a PCE of 20% exceeds 343 K (24), temperature effects cannot be ignored. Previous studies have shown that temperature plays a notable effect on solar efficiency such as decreasing the open-circuit voltage Voc of MAPbI₃-based solar cells from 1.01 to 0.83 V as the temperature increases from 300 to 360 K (25). In part, V_{oc} drop could be due to the renormalization of the band gap of MAPbI₃ with temperature, which is of the order of 30 to 40 meV in the temperature range of solar cell operation (26-29). In addition, the degradation of PCE with temperature could be due to enhancements in the inelastic scattering between defect and charged carriers, as these are mediated by electron-phonon coupling. Although a couple of studies have recently investigated nonradiative processes in MAPbI₃ (30, 31), a comprehensive understanding of how defects affect the *e-h* recombination in the MHPs and how these differ from traditional semiconductors is still lacking.

Here, we study, in detail, the interplay between nonradiative e-h recombination processes and point defects in MAPbI $_3$ using a nonadiabatic molecular dynamics (NAMD) approach. Considering only the intrinsic point defects in MAPbI $_3$, there are three types of vacancy defects (I_V , Pb_V , and MA_V), three interstitial defects (I_i , MA_i , and Pb_i), and six antisite defects (I_{MA} , MA_I , Pb_I , I_{Pb} , Pb_{MA} , and MA_{Pb} , where A_B indicates that A is substituted by B). Among these 12 types, we focus our study on defects that have low formation energies and thus are abundant during synthesis. These include I interstitial (I_i), MA substituted by I (MA_I) or Pb (MA_{Pb}), Pb vacancy (Pb_V), and I vacancy (I_V) (I_V). While these defects are found to display distinctly different electronic structures by either having mid-gap or shallow p- or p-type defect states, we show that surprisingly these defects do not accelerate e-h recombination. We find that the charge recombination for the I_i

system is even suppressed by a factor of 2 compared to the pristine system. We further find that for both the pristine and defective systems, the photogenerated carriers are only coupled with low-frequency phonons, which notably decrease the nonadiabatic coupling (NAC) between the donor and acceptor states. Therefore, both the pristine and defective systems have a long e-h recombination time. We propose that these conclusions are general for all hybrid organic-inorganic perovskite solar cells and may extend to other semi-conductors with low-frequency lattice phonons.

RESULTS

Before investigating the *e-h* recombination dynamics, it is instructive to study the static (0 K) electronic structure of the different defective systems. The optimized atomic structure of the five defects and their corresponding density of states (DOS) are shown in Fig. 1. For comparison, we also show the results of the pristine system. One can see that Ii and Pby introduce shallow defect states near the valence band maximum (VBM), while MA_{Pb} and I_V introduce shallow defect states near the conduction band minimum (CBM). MAI, on the other hand, introduces a deep defect state located 1.4 eV above the VBM. On the basis of the electronic structure, we can regard I_i and Pb_V as p-type defects as well as I_V and MA_{Pb} as n-type defects, whereas MAI can be considered as a neutral defect. The calculated electronic structures of these defects are consistent with our previous study using a larger supercell and spin-orbit coupling (SOC) correction (7). Further, we verified that the results are consistent with the Heyd-Scuseria-Ernzerhof (HSE06) + SOC electronic structure, except for I_i, in which we find the defect shallow state obtained with Perdew-Burke-Ernzerhof (PBE) to split into a shallow and deep state (fig. S3) (17). Nevertheless, as we discuss in the Supplementary Materials, this does not appreciably affect the recombination rates (section S2).

Electron-phonon interactions can have notable effects on the electronic structure of the system. Figure 2 shows the time evolution

of the frontier and defect energy levels at 300 K. Only I_i and MA_{Pb} have shallow defect states close to the VBM and CBM, respectively (Fig. 2, A and C), while MA_I , Pb_V , and I_V introduce defect states in the band gap (Fig. 2, B, D, and E). Further, as can be seen from the figure, the modulations of the defect states along the molecular dynamics (MD) trajectory are more notable compared to those of the VBMs and CBMs. This is somewhat expected, given that the defect state is associated with a number of broken bonds that are less rigid during the MD (fig. S4).

Following a photoexcitation, the electron-phonon coupling can induce a direct nonradiative recombination of electrons and holes on CBM or VBM or via a by-defect nonradiative recombination mediated by the defect states, as is shown schematically in Fig. 3A. The direct path commences with an electron (hole) hopping to the VBM (CBM), followed by *e-h* recombination. The by-defect path is more complex with different nonradiative carrier relaxation pathways. For example, a captured excited hole by the defect either can recombine with an electron in place after hopping to the conduction band or can even thermally escape and relax back to the VBM without any recombination if the energy barrier could be overcome by thermal fluctuations. Similar pathways exist for the electron, as shown in Fig. 3A. The overall nonradiative *e-h* recombination that deteriorates the efficiency of the solar cell is the result of the competition between all of these processes, which are described using the NAMD framework. Radiative and Auger *e-h* recombinations are not discussed in this work.

Figure 3B depicts the direct and by-defect recombination rates from the NAMD dynamics following a photoexcitation after evolving the system for 2 ns. Figure 3 (C and D) depicts the time changes of the direct and by-defect rates over 2 ns for the two pathways, which are used to estimate the e-h lifetime. For the pristine system, Fig. 3B shows that ~19% of the different sampled e-h trajectories terminate with a nonradiative recombination with an estimated e-h lifetime of ~11 ns. Despite the distinct nature of the defect states, Fig. 3B shows that there is no notable acceleration of charge recombination in the

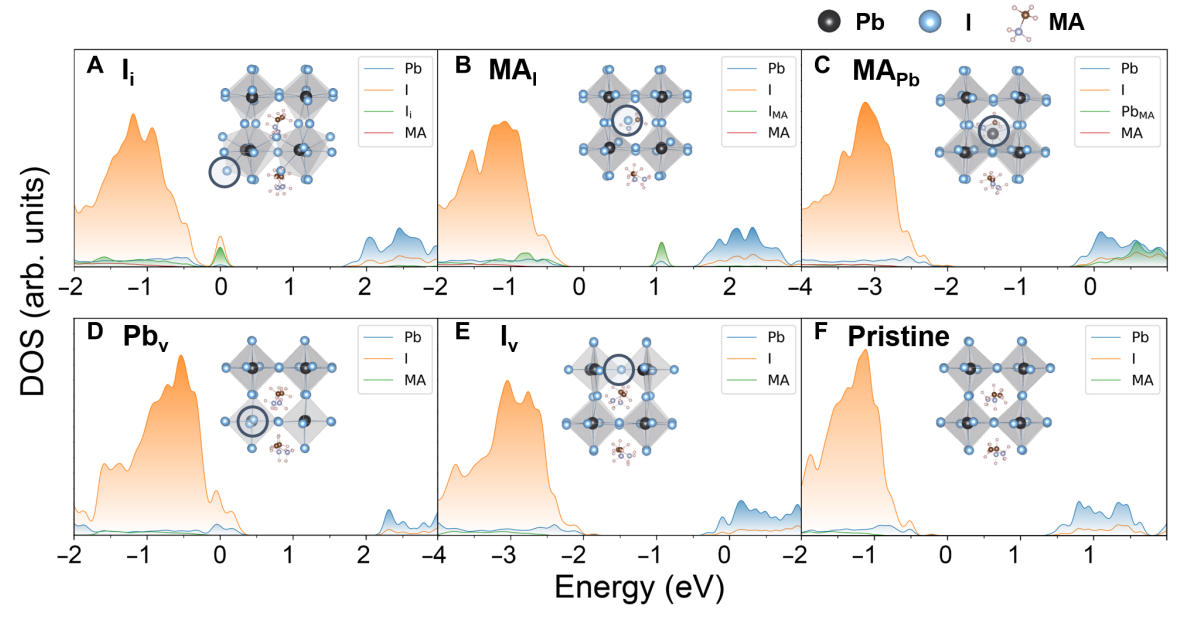


Fig. 1. Atom-projected DOS for different defective and pristine MAPbl₃. (A to F) Defective and Pristine systems of MAPbl₃. The energy reference is located at the Fermi level. Inset shows corresponding atomic structure, with blue circle indicating the defect location.

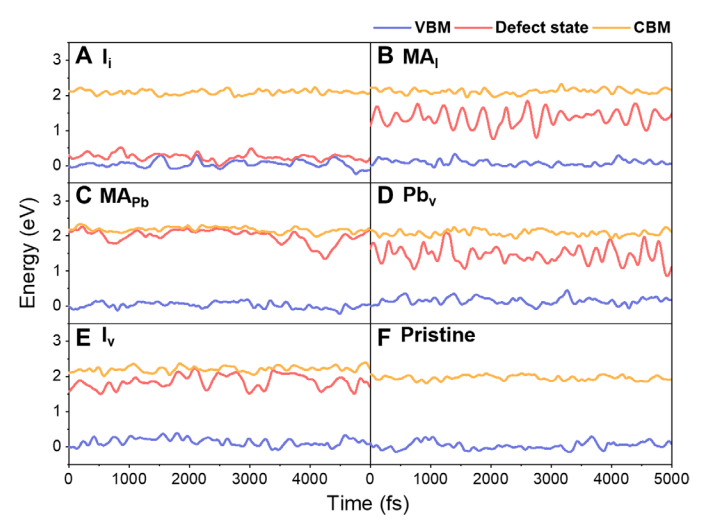


Fig. 2. The time evolution of the VBM, the CBM, and the defect state for MAPbI₃ systems at 300 K. (A to F) Defective and Pristine systems of MAPbI₃. The energy reference is located at the VBM of the initial configuration.

defected systems in comparison to the pristine one, even after incorporating the new by-defect carrier pathways. The charge recombination rates are found to be ~17% (MA_{Pb}), 17% (MA_I), 24% (I_V), and 25% (MA_I), which are comparable with the rate obtained in the pristine system. In addition, the corresponding charge recombination time scales are similar to the pristine system. In contrast to the other defects, surprisingly, I_i is found to notably suppress the recombination rate to ~9%, which is less than half the value of the pristine MAPbI₃. This results in a longer *e-h* recombination lifetime of ~23 ns for I_i. The slower charge recombination time reduces electronic energy dissipation into phonons and enhances photon-to-electron conversion efficiency.

The predicted NAMD nanosecond time scales of the e-h recombination are underestimated compared with the lifetime measured experimentally in neat MAPbI₃ (3, 4, 32). This is likely due to confinement effects introduced by the small unit cell, which limits the carriers' diffusion and thus increases the probability of scattering and recombination. Given the computational cost of first-principles calculations, it is not practical to simulate realistic system size that would be of the order of $20 \times 20 \times 20$ supercell with 40,000 atoms. To assess finite size effects, we used a larger $2 \times 2 \times 2$ supercell with 384 atoms. Figure S1 shows that the *e-h* recombination time increases with systems size from 11 to 64 ns. Assuming that the e-h scattering probability is linearly proportional to the volume of the unit cell, we can estimate the lifetime of the $20 \times 20 \times 20$ supercell to be of the order of 60 µs. Although this time scale is in line with recent experimental values, more investigations are needed to accurately determine the lifetime. Although issues related to finite size effects are shown in fig. S1, we show in the Supplementary Materials that the relative magnitude in the e-h recombination rates between the pristine and defective MAPbI₃ is less sensitive to the unit cell size (section S1).

As have been discussed in the previous studies (33, 34), the *e-h* recombination rate is strongly dependent on the NAC between the donor and acceptor states. The NAC matrix element d_{jk} can be expressed as

$$d_{jk} = \left\langle \varphi_j \mid \frac{\partial}{\partial t} \mid \varphi_k \right\rangle = \frac{\left\langle \varphi_j \mid \nabla_R H \mid \varphi_k \right\rangle}{\epsilon_k - \epsilon_j} \dot{R} \tag{1}$$

Here, H is the Kohn-Sham (KS) Hamiltonian; φ_j , φ_k , ϵ_j , and ϵ_k are the wave functions and eigenvalues for donor and acceptor states j and k, respectively; and \dot{R} is the nuclear velocity (34). The first equality in Eq. 1 shows that the NAC is due to the overlap between two orbitals at adjacent ionic time steps along the MD trajectory. The second equivalent representation of the NAC matrix in Eq. 1 shows more clearly that d_{jk} depends on the energy difference $\epsilon_k - \epsilon_j$, the electron-phonon coupling term $\langle \varphi_j \mid \nabla_R H \mid \varphi_k \rangle$, and the nuclear velocity term \dot{R} . In the e-h recombination NAMD dynamics, the donor and acceptor states include the CBM, the VBM, and the defect state. Because the NAC varies with atomic configurations, we report in Table 1 the root mean square NAC values between the different states to quantify the coupling strength along the MD trajectory. As we will argue next, the average NAC can provide a good understanding of the e-h dynamics reported in Fig. 3.

The NAC between CBM and VBM of the pristine system is 0.69 meV, which is larger than all corresponding values for the defective systems as shown in Table 1. This indicates that the recombination of free carriers in the CBM and VBM is suppressed in the defective systems. However, as shown in Fig. 3 (B and C), the probability for recombination via the direct path in the defected systems is markedly smaller than that of the pristine one. This apparent inconsistency is because the NAC between defect with either CBM or VBM is larger by one order of magnitude than that between CBM and VBM. Therefore, the electron or hole is likely to be trapped by the defect, and thus, the charge dynamics in these defective systems are mainly driven by the by-defect path and concomitantly restraining recombination via the direct path.

Further, examining the coupling values for the by-defect route in Table 1, we see that while for MA_{Pb}, Pb_V, and I_V, the NAC matrix element between the CBM and the defect state is relatively large (10.25, 3.98, and 7.03 meV, respectively), the corresponding NAC values between the defect state and the VBM are notably smaller (0.56, 0.35, and 0.59 meV, respectively). These NAC values suggest that MA_{Pb}, Pb_V, and I_V defects will capture an excited electron with a high probability but are less likely to trap a hole. Therefore, the e-h recombination due to the defect states will not be facile, with the hole capture process being rate limiting. Similarly, the charge recombination for Ii systems is also hindered because the defect has a weak coupling for the electron despite being a hole trap state. For the neutral MAI defect, the NAC matrix elements between the VBM (CBM) and the defect state are 0.46 (1.25) meV, which are of similar magnitude. Therefore, the MA_I system with the mid-gap state is a potential e-h recombination center. As shown in Fig. 3B, the by-defect charge recombination in MA_I is the fastest among the five systems we have investigated. However, the recombination rate is not appreciably accelerated because of the small NAC values (0.46 meV). From this analysis, it can be seen that the by-defect e-h recombination is mostly determined by the smallest NAC among the VBM, the CBM, and the defect state. This is referred to as effective NAC. In summary, regardless of the defect type, the effective NAC for charge recombination in the defective MAPbI₃ systems is smaller than that of the pristine system.

The NACs between different states strongly depend on the phonon excitation and electron-phonon coupling, which can be understood from the fluctuations in the band energies shown in Fig. 2. The phonon excitations that coupled to the electron subsystem can be determined by examining the (normalized) autocorrelation function $C(t) = \langle E(t)E(0) \rangle / \langle E(0)E(0) \rangle$ for the state energy E(t), where the

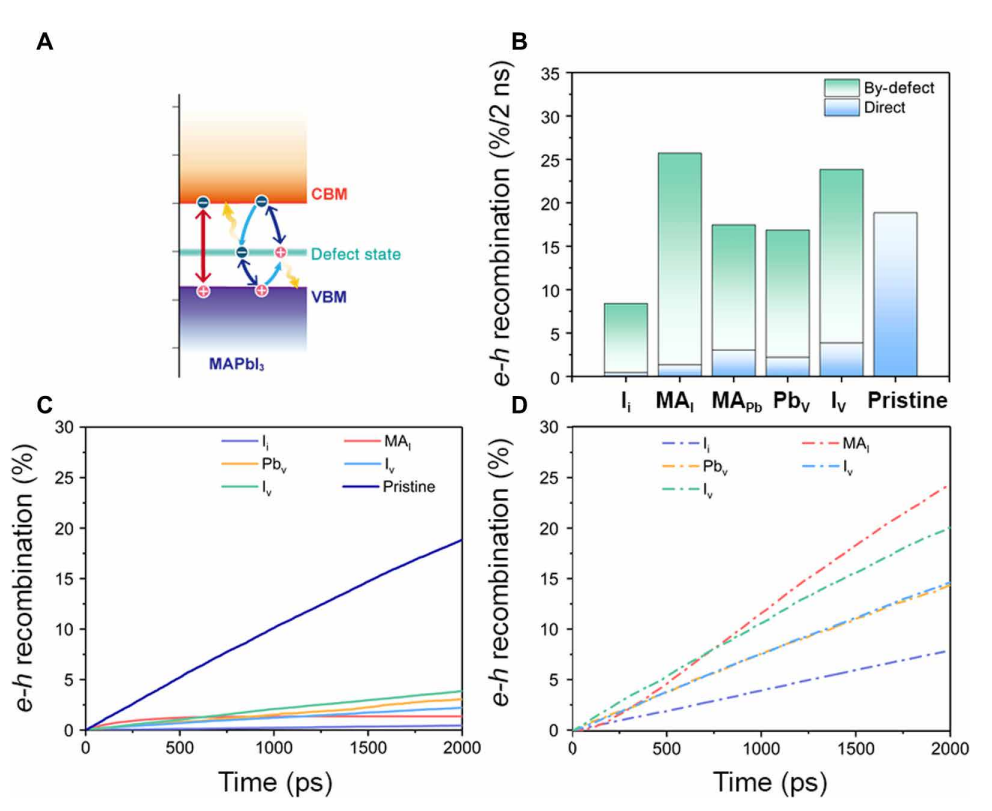


Fig. 3. The *e-h* recombination process in MAPbl₃ systems. (A) Schematic map of the direct and by-defect *e-h* recombination processes. (B) *e-h* recombined percentage for different systems after 2 ns. The direct and by-defect *e-h* recombined percentages are shown by blue and green color bars. (C and D) Time-dependent *e-h* recombined percentage for different systems. The direct and by-defect *e-h* recombined percentage is shown in (C) and (D), respectively.

	NAC (meV)		
	VBM-CBM	VBM-defect	CBM-defect
Pristine	0.69		
l _i	0.56	7.17	0.58
MA _I	0.55	0.46	1.25
MA _{Pb}	0.57	0.56	10.25
Pb _v	0.63	0.35	3.98
l _v	0.63	0.59	7.03

brackets $\langle ... \rangle$ indicate canonical averaging. A rapid decay of C(t) from 1 to 0 indicates that the fluctuations are driven by many vibrations, while a periodic oscillatory behavior indicates that few modes couple to the electron subsystem. Figure 4 shows the Fourier transform of C(t) for the VBM, the CBM, and the defect state energies, which is generally used to analyze the phonon frequencies due to electron-phonon coupling (34). First, one can see that for all the different systems, the frequencies of the dominant phonon modes are below $100~{\rm cm}^{-1}$. The low-frequency phonon modes are associated with heavy mass atoms that have appreciably small nuclear velocities and consequently result in small NAC as seen from Eq. 1. These low-frequency phonon modes are the optical phonons contributed by the inorganic Pb-I lattice (35, 36). On the other hand, the absence

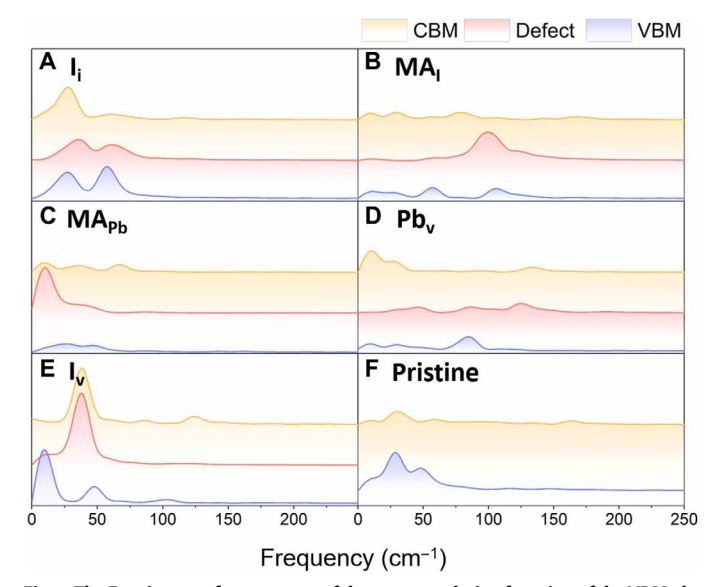


Fig. 4. The Fourier transform spectra of the autocorrelation function of the VBM, the CBM, and the defect state energies. (A to F) Defective and Pristine systems of MAPbl₃.

of appreciable peaks in the 150 to 3500 cm $^{-1}$ range indicates that MA molecular vibrations are not coupled with the CBM, the VBM, or defect states. Note that our MD trajectory (~10 ps) is long enough to capture the rotational dynamics of MA that has a ~7 ps time scale at 300 K (*37*). Further, the negligible role of MA, if any, in influencing

the NAC is justified because MA does not contribute directly to the frontier orbitals (38) or even to the defect states (vide infra). In addition, this is consistent with conclusions drawn before using a similar NAMD approach (31).

Figure 5 shows the distribution of the electron density for the frontier and defect orbitals for a configuration extracted from the MD trajectory. For the pristine system, in agreement with previous investigations, the VBM and CBM are distributed mainly on I and Pb atoms, respectively (38). As seen from Fig. 5, the native defects in MAPbI₃ localize the CBM and VBM electron distribution due to strong distortions in the lattice. This localization, in turn, decreases the overlap between the orbitals at neighboring time steps, which explains the decrease in the NAC (see Table 1). The defect states are also localized as shown in Fig. 5, which also reduce the NAC, thus supporting the relatively small effective NAC values for KS orbitals that are not close in energy. In the case of I_i, Fig. 5A shows that, near an iodine interstitial, the electron density is depleted for the VBM and CBM but enhanced for the defect state. This charge redistribution appreciably decreases the NAC, which thus suppresses the e-hrecombination rate. During the MD, there can be strongly disordered structures, as have been discussed in previous investigations (39), which also reduce the NAC.

To explore the impact of SOC on our results, we have extracted on the order of 10 different configurations from the MD trajectory and computed the NAC using the adiabatic self-consistent spinor wave function, $\psi(r,t) = \begin{pmatrix} \varphi_+(r,t) \\ \varphi_-(r,t) \end{pmatrix}$, where φ_+ and φ_- are the two spinor

A I

B MA

C MA

Pb

F Pristine

Fig. 5. Orbital spatial distribution of the VBM, the CBM, and the defect states of the MAPbl $_3$ systems. (A to F) Defective and Pristine systems. Orange circles indicate the defect location.

components. The configurations are selected such that their NAC matrix elements with PBE are similar to the average values shown in Table 1 to capture the most observed behavior. Using the spinor basis sets, we computed the NAC using the Hammes-Schiffer and Tully equation (40).

$$d_{jk} = \left\langle \psi_j | \frac{\partial}{\partial t} | \psi_k \right\rangle \tag{2}$$

$$= \frac{1}{2dt} (\langle \psi_j(r,t) \mid \psi_k(r,t+dt) \rangle - \langle \psi_j(r,t+dt) \mid \psi_k(r,t) \rangle)$$
 (3)

$$= \frac{1}{2dt} \langle \langle \varphi_{j+}(r,t) \mid \varphi_{k+}(r,t+dt) \rangle + \langle \varphi_{j-}(r,t) \mid \varphi_{k-}(r,t+dt) \rangle \quad (4)$$

$$-\langle \varphi_{j+}(r,t+dt) \mid \varphi_{k+}(r,t) \rangle - \langle \varphi_{j-}(r,t+dt) \mid \varphi_{k-}(r,t) \rangle$$

As we show in table S1, the NAC matrix elements with PBE + SOC are much larger than those obtained using PBE, which is understood because the band gap with PBE + SOC is notably underestimated compared to the PBE band gap, and the NAC is inversely proportional to eigenvalue differences as seen in Eq. 1. However, despite this, we can see that the relative values between the NAC PBE + SOC and PBE matrix elements are similar, suggesting that our findings will not be affected by ignoring SOC. For example, from the NAC values associated with the defect state, we conclude that $MA_{Pb}, Pb_{V},$ and I_{V} are only electron trap states and I_{i} has a hole trap state, while MA_{I} could be an $\emph{e-h}$ recombination center but with a weak recombination rate. In addition, the NAC for the direct recombination path is similar or smaller than that of the pristine system. These conclusions are also collaborated by the orbital distribution that includes the effect of SOC shown in fig. S2.

DISCUSSION

It is useful to contrast MAPbI₃ with a traditional semiconductor such as TiO_2 . The by-defect *e-h* recombination process shown in Fig. 3 is also active in TiO₂. However, in strong contrast to TiO₂, in MAPbI₃, the rates are not accelerated as compared with the pristine system. In rutile TiO₂, Zhang et al. (33) showed that non-isoelectronic Cr-N substitutions for Ti-O would induce a delocalized impurity phonon mode (section S7) with strong coupling with neighboring atoms, which notably enhances the NAC from 1.5 meV for the undoped system to ~25 meV. On the other hand, for isoelectronic V-N codoped substitution, the impurity phonon modes are localized, and the recombination rates are not different from the undoped system. Similar analysis on the phonon localization in our system, as seen in figs. S5 and S6, shows that defect-related atoms have 20% contributions to different phonon modes. This is indicative that the defectrelated phonon modes that couple to the electron subsystem are also delocalized, which is similar to the non-isoelectronic doping in TiO₂. However, in contrast to the TiO₂ systems, the NAC for the MAPbI₃ systems is not enhanced, and hence, we do not see an acceleration of the e-h recombination. The main reason for the differences with TiO2, and consequently for the strong defect tolerance in MAPbI₃, is that the phonon modes that drive the NAC have relatively low frequencies below 100 cm⁻¹, as shown in Fig. 4. In contrast, in pristine TiO₂, the CBM and VBM couple with phonons above 500 cm⁻¹, while the defect states couple with impurity phonons above 900 and 800 cm⁻¹ for the isoelectronic and non-isoelectronic substitutions, respectively (33).

The notable differences in the phonons between TiO₂ and MAPbI₃ can be correlated with their bulk moduli. The bulk modulus of MAPbI₃ is smaller than typical metal oxides like TiO₂ by one order of magnitude (41–45). The bulk modulus is determined by the second derivative of the energy of the system versus the volume change, which makes it sensitive to the lattice phonon modes (46, 47). In MAPbI₃, the small bulk modulus can be attributed to the low-frequency phonon modes of the inorganic lattice. We propose that the "soft" nature (small bulk moduli) of MAPbI₃ is correlated with the weak NAC and hence prolonged *e-h* recombination lifetimes. These conclusions are likely applicable to other semiconductors with small bulk moduli including other hybrid organic-inorganic perovskites.

For completeness, the defect tolerance in MAPbI₃ could also be due to additional factors such as the formation of large polarons, as well as reduced Coulomb screening based on local symmetry breaking and dynamic ferroelectric effect (18, 42, 43, 44, 48, 49). As argued recently, on the basis of direct time-domain view, large polarons form in MAPbBr₃ and CsPbBr₃ due to deformations in PbBr₃ lattice regardless of the cation, which is also in line with our findings that the organic molecule has little effect, if any, on the NAC. In addition, recently, Meggiolaro *et al.* (17) argued that the peculiar iodine redox chemistry could explain the defect tolerance, as this will promote faster hole trapping compared to electron trapping.

The NAMD simulation results of MAPbI₃ are not consistent with the well-known SRH mechanism proposed in the 1950s (21), which has been widely used to predict the *e-h* recombination rates based on the electronic structures of defects (section S6). By only considering the carrier concentration and the energy of the defect state, SRH predicts that deep defect states in the middle of the band gap behave as an e-h recombination center. On the contrary, if the defect states are close to the VBM or CBM, then the electron/hole will be easily trapped, and charge recombination will not be accelerated. Here, our results show that charge recombination is not accelerated in the presence of native defects regardless of the location of the defect state in the band gap. As we showed in this study, the breakdown of SRH is because the electron-phonon coupling, which is the dominating factor of the nonradiative charge recombination, is not considered in the original SRH model. Our results suggest that in halide perovskites, the coupling with the low-frequency lattice phonons efficiently suppresses the charge recombination and the simple SRH model is not sufficient. These findings call for careful time-resolved experimental measurements to benchmark different theoretical methods and models.

To summarize, using time-dependent ab initio NAMD simulation, we have investigated the e-h recombination dynamics of five stable native point defects in MAPbI_3. Although the electronic structure associated with the defect states is distinct in these different systems, we have not observed the acceleration of charge recombination. On the contrary, I_i suppresses the e-h recombination. Our analyses show that the strong defect tolerance in MAPbI_3 is due to the low-frequency phonons contributed by the inorganic lattice that are weakly coupled to the organic molecules. In MAPbI_3, only low-frequency phonon modes can be excited, resulting in a weak NAC between the states. We propose that these conclusions are also applicable to other hybrid perovskites, which share with MAPbI_3 similar properties, in particular, a small bulk modulus value. These findings are important in the future design of functional semi-conducting materials for solar energy conversion.

MATERIALS AND METHODS

The ab initio NAMD simulations were performed using the Hefei-NAMD code (33, 34, 50, 51) within real-time time-dependent KS equation framework (34). We used VASP (Vienna Ab initio Simulation Package) (52) to optimize the structure at T = 0 K, obtain the nuclear trajectory, and calculate the KS orbitals that are needed to compute the NAC for NAMD simulations. The electron-nuclei interactions were described using the projector augmented-wave method (53). The tetragonal phase is represented using a $(\sqrt{2} \times \sqrt{2} \times 2)$ unit cell of the cubic phase with lattice constants a = 8.8 Å and c = 12.685 Å. We used a $4 \times 4 \times 2$ Monkhorst-Pack **k**-point mesh to sample the Brillouin zone. After the geometry optimization, we used velocity rescaling to bring the system's temperature to 300 K; a 10-ps microcanonical ab initio MD trajectory was then generated with a time step of 1 fs. Using the MD trajectory, the NAMD results were based on averaging over 100 different initial configurations. For each chosen structure, we sampled 500 trajectories for 2 ns. Decoherence-induced surface-hopping method was used to account for quantum decoherence (section S5) (54). In general, shorter decoherence time leads to slower dynamics, as exemplified by the quantum Zeno effect in which the dynamics stop in the limit of infinitely fast decoherence (55).

The density functional theory (DFT) calculations PBE (56) exchange-correlation functional and accounts for van der Waals interactions that are important for MHP systems (36) using DFT-D3 (57). Because of the presence of heavy Pb atoms, the inclusion of SOC is important to correctly describe the band structure (58) and even the stability (7) of MAPbI₃. Because semi-local functionals generally underestimate the band gap, previous studies have shown that PBE without SOC yields band gaps in good agreement with experiments and high-level SOC + GW calculations due to a cancelation of the two effects (59). NAMD investigations are computationally expensive, requiring solving KS equations a few thousand times. Thus, it is not practical to use SOC + GW calculations in the NAMD simulations. Instead, here, we simply used the PBE functional as performed in previous NAMD studies on MAPbI₃ (30, 31). However, given the importance of SOC corrections, we further used calculations with SOC to assess their impact on our results (section S3). In addition, we investigated the effects of using the hybrid exchange-correlation functional HSE06 with 43% exact exchange, as proposed in (17). When coupled to SOC, this modified HSE06 yields electronic structure similar to the high-level GW-SOC (59). The NAC values obtained with PBE-SOC and HSE06-SOC are summarized in tables S1 and S2.

In NAMD simulations, the NAC was numerically evaluated from the overlap between two KS orbitals at adjacent ionic time steps (40). Because the adiabatic KS orbitals along the trajectory can differ by an arbitrary random phase due to the different mathematical methods, the overlap of the KS orbitals is not uniquely determined, which leads to a "phase consistency" problem. If not accounted for correctly, then this random phase will result in an erroneous evaluation of the NAC and subsequently cause serious problems in the numerical integration of the NAMD equations, making the NAMD results not reproducible. In our calculations, we applied the phase correction similar to the method introduced by Akimov (60).

SUPPLEMENTARY MATERIALS

 $Supplementary\ material\ for\ this\ article\ is\ available\ at\ http://advances.sciencemag.org/cgi/content/full/6/7/eaaw7453/DC1$

Section S1. Impurity concentration Section S2. Spin-orbit coupling

SCIENCE ADVANCES | RESEARCH ARTICLE

- Section S3. The validity of using PBE functional
- Section S4. Electronic structure change induced by electron-phonon interactions
- Section S5. Decoherence effects
- Section S6, SRH model
- Section S7. The impurity phonon localization
- Section S8. Phonon effects on the NAMD of electronic states
- Fig. S1. The time-dependent e-h recombined percentage for different systems.
- Fig. S2. The orbital distribution with SOC of the VBM, the CBM, and the defect states for pristine and different defective MAPbl $_3$ systems.
- Fig. S3. Electronic state levels of CBM spinors (blue line), VBM spinors (purple line), and defect spinors (orange line) of the different MAPbl $_3$ systems for a single configuration at 300 K.
- Fig. S4. Electron-phonon interactions induce electronic structure changes for Pb_{ν} defective MAPbl $_3$ at 300 K.
- Fig. S5. The total DOS of phonons (blue) and projected DOS of impurity phonons (orange) of the pristine and different defective MAPbl $_3$ systems.
- Fig. S6. The ratio of impurity phonon modes to the total phonon modes of the pristine and different defective MAPbl $_3$ systems.
- Table S1. The NAC between the spinor of the VBM, the CBM, and the defect states for different systems when including the effect of SOC.
- Table S2. The NAC between the spinor states of the VBM, the CBM, and the defect states for different systems calculated at the PBE and HSE06 + SOC.
- Table S3. The pure dephasing time between the VBM, the CBM, and the defect states for different systems.

References (61-69)

REFERENCES AND NOTES

- W. J. Yin, T. T. Shi, Y. F. Yan, Unique properties of halide perovskites as possible origins of the superior solar cell performance. Adv. Mater. 26, 4653–4658 (2014).
- G. Grancini, S. Marras, M. Prato, C. Giannini, C. Quarti, F. De Angelis, M. De Bastiani, G. E. Eperon, H. J. Snaith, L. Manna, A. Petrozza, The impact of the crystallization processes on the structural and optical properties of hybrid perovskite films for photovoltaics. *J. Phys. Chem. Lett.* 5, 3836–3842 (2014).
- G. C. Xing, N. Mathews, S. Y. Sun, S. S. Lim, Y. M. Lam, M. Grätzel, S. Mhaisalkar, T. C. Sum, Long-range balanced electron- and hole-transport lengths in organic-inorganic CH₃NH₃Pbl₃. Science 342, 344–347 (2013).
- S. D. Stranks, G. E. Eperon, G. Grancini, C. Menelaou, M. J. P. Alcocer, T. Leijtens, L. M. Herz, A. Petrozza, H. J. Snaith, Electron-hole diffusion lengths exceeding 1 micrometer in an organometal trihalide perovskite absorber. *Science* 342, 341–344 (2013).
- W.-J. Yin, T. T. Shi, Y. F. Yan, Unusual defect physics in CH₃NH₃Pbl₃ perovskite solar cell absorber. Appl. Phys. Lett. 104, 063903 (2014).
- J. Kim, S.-H. Lee, J. H. Lee, K.-H. Hong, The role of intrinsic defects in methylammonium lead iodide perovskite. J. Phys. Chem. Lett. 5, 1312–1317 (2014).
- W. T. Shan, W. A. Saidi, Segregation of native defects to the grain boundaries in methylammonium lead iodide perovskite. J. Phys. Chem. Lett. 8, 5935–5942 (2017).
- Y. G. Guo, Q. Wang, W. A. Saidi, Structural stabilities and electronic properties of high-angle grain boundaries in perovskite cesium lead halides. *J. Phys. Chem. C* 121, 1715–1722 (2017).
- S. I. Seok, M. Grätzel, N.-G. Park, Methodologies toward highly efficient perovskite solar cells. Small 14, 1704177 (2018).
- Y. X. Zhao, K. Zhu, Organic-inorganic hybrid lead halide perovskites for optoelectronic and electronic applications. Chem. Soc. Rev. 45, 655–689 (2016).
- M. A. Green, K. Emery, Y. Hishikawa, W. Warta, E. D. Dunlop, Solar cell efficiency tables (version 45). Prog. Photovolt. 23, 1–9 (2015).
- W. Shockley, H. J. Queisser, Detailed balance limit of efficiency of p-n junction solar cells. J. Appl. Phys. 32, 510–519 (1961).
- W. E. I. Sha, X. G. Ren, L. Z. Chen, W. C. H. Choy, The efficiency limit of CH₃NH₃Pbl₃ perovskite solar cells. *Appl. Phys. Lett.* 106, 221104 (2015).
- K. Tvingstedt, O. Malinkiewicz, A. Baumann, C. Deibel, H. J. Snaith, V. Dyakonov, H. J. Bolink, Radiative efficiency of lead iodide based perovskite solar cells. Sci. Rep. 4, 6071 (2014).
- J. M. Ball, A. Petrozza, Defects in perovskite-halides and their effects in solar cells. Nat. Energy 1. 16149 (2016).
- 16. W. Tress, N. Marinova, O. Inganas, M. K. Nazeeruddin, S. M. Zakeeruddin, M. Graetzel, Predicting the open-circuit voltage of CH₃NH₃Pbl₃ perovskite solar cells using electroluminescence and photovoltaic quantum efficiency spectra: The role of radiative and non-radiative recombination. Adv. Energy Mater. 5, 1400812 (2015).
- D. Meggiolaro, S. G. Motti, E. Mosconi, A. J. Barker, J. Ball, C. A. R. Perini, F. Deschler, A. Petrozza, F. De Angelis, Iodine chemistry determines the defect tolerance of lead-halide perovskites. *Energy Environ. Sci.* 11, 702–713 (2018).
- Y. Chen, H. T. Yi, X. Wu, R. Haroldson, Y. N. Gartstein, Y. I. Rodionov, K. S. Tikhonov, A. Zakhidov, X. Y. Zhu, V. Podzorov, Extended carrier lifetimes and diffusion in hybrid

- perovskites revealed by Hall effect and photoconductivity measurements. *Nat. Commun.* **7.** 12253 (2016).
- T. Leijtens, G. E. Eperon, A. J. Barker, G. Grancini, W. Zhang, J. M. Ball, A. R. S. Kandada, H. J. Snaith, A. Petrozza, Carrier trapping and recombination: The role of defect physics in enhancing the open circuit voltage of metal halide perovskite solar cells. *Energy Environ. Sci.* 9, 3472–3481 (2016).
- D. W. deQuilettes, S. M. Vorpahl, S. D. Stranks, H. Nagaoka, G. E. Eperon, M. E. Ziffer, H. J. Snaith, D. S. Ginger, Impact of microstructure on local carrier lifetime in perovskite solar cells. *Science* 348, 683–686 (2015).
- W. Shockley, W. T. Read Jr., Statistics of the recombinations of holes and electrons. Phys. Rev. 87, 835–842 (1952).
- J. Kang, L. W. Wang, High defect tolerance in lead halide perovskite CsPbBr₃.
 J. Phys. Chem. Lett. 8, 489–493 (2017).
- H. Huang, M. I. Bodnarchuk, S. V. Kershaw, M. V. Kovalenko, A. L. Rogach, Lead halide perovskite nanocrystals in the research spotlight: Stability and defect tolerance. ACS Energy Lett. 2. 2071–2083 (2017).
- E. Skoplaki, A. G. Boudouvis, J. A. Palyvos, A simple correlation for the operating temperature of photovoltaic modules of arbitrary mounting. Sol. Energy Mater. Sol. Cells 92, 1393–1402 (2008).
- H. Zhang, X. Qiao, Y. Shen, T. Moehl, S. M. Zakeeruddin, M. Grätzel, M. Wang, Photovoltaic behaviour of lead methylammonium triiodide perovskite solar cells down to 80 K. J. Mater. Chem. A 3, 11762–11767 (2015).
- B. J. Foley, D. L. Marlowe, K. Y. Sun, W. A. Saidi, L. Scudiero, M. C. Gupta, J. J. Choi, Temperature dependent energy levels of methylammonium lead iodide perovskite. *Appl. Phys. Lett.* **106**, 243904 (2015).
- R. L. Milot, G. E. Eperon, H. J. Snaith, M. B. Johnston, L. M. Herz, Temperature-dependent charge-carrier dynamics in CH₃NH₃Pbl₃ perovskite thin films. *Adv. Funct. Mater.* 25, 6218–6227 (2015).
- W. A. Saidi, S. Ponce, B. Monserrat, Temperature dependence of the energy levels of methylammonium lead iodide perovskite from first-principles. J. Phys. Chem. Lett. 7, 5247–5252 (2016).
- W. A. Saidi, A. Kachmar, Effects of electron–phonon coupling on electronic properties of methylammonium lead iodide perovskites. J. Phys. Chem. Lett. 9, 7090–7097 (2018).
- R. Long, J. Liu, O. V. Prezhdo, Unravelling the effects of grain boundary and chemical doping on electron–hole recombination in CH₃NH₃Pbl₃ perovskite by time-domain atomistic simulation. *J. Am. Chem. Soc.* 138, 3884–3890 (2016).
- W. Li, J. Liu, F.-Q. Bai, H.-X. Zhang, O.-V. Prezhdo, Hole trapping by iodine interstitial defects decreases free carrier losses in perovskite solar cells: A time-domain ab initio study. ACS Energy Lett. 2, 1270–1278 (2017).
- Y. Yamada, T. Nakamura, M. Endo, A. Wakamiya, Y. Kanemitsu, Photocarrier recombination dynamics in perovskite CH₃NH₃Pbl₃ for solar cell applications. J. Am. Chem. Soc. 136, 11610–11613 (2014).
- L. L. Zhang, Q. J. Zheng, Y. Xie, Z. G. Lan, O. V. Prezhdo, W. A. Saidi, J. Zhao, Delocalized impurity phonon induced electron–hole recombination in doped semiconductors. *Nano Lett.* 18, 1592–1599 (2018).
- Q. Zheng, W. Chu, C. Zhao, L. Zhang, H. Guo, Y. Wang, X. Jiang, J. Zhao, Ab initio nonadiabatic molecular dynamics investigations on the excited carriers in condensed matter systems. Wiley Interdiscip. Rev. 9, e1411 (2019).
- C. Quarti, G. Grancini, E. Mosconi, P. Bruno, J. M. Ball, M. M. Lee, H. J. Snaith, A. Petrozza, F. De Angelis, The Raman spectrum of the CH₃NH₃Pbl₃ hybrid perovskite: Interplay of theory and experiment. *J. Phys. Chem. Lett.* 5, 279–284 (2014).
- W. A. Saidi, J. J. Choi, Nature of the cubic to tetragonal phase transition in methylammonium lead iodide perovskite. J. Chem. Phys. 145, 144702 (2016).
- S. Govinda, B. P. Kore, M. Bokdam, P. Mahale, A. Kumar, S. Pal, B. Bhattacharyya, J. Lahnsteiner, G. Kresse, C. Franchini, A. Pandey, D. D. Sarma, Behavior of methylammonium dipoles in MAPbX₃ (X = Br and I). *J. Phys. Chem. Lett.* 8, 4113–4121 (2017).
- F. Brivio, A. B. Walker, A. Walsh, Structural and electronic properties of hybrid perovskites for high-efficiency thin-film photovoltaics from first-principles. APL Mater. 1, 042111 (2013).
- M. L. Agiorgousis, Y. Y. Sun, H. Zeng, S. B. Zhang, Strong covalency-induced recombination centers in perovskite solar cell material CH₃NH₃Pbl₃. *J. Am. Chem. Soc.* 136. 14570–14575 (2014).
- S. Hammes-Schiffer, J. C. Tully, Proton transfer in solution: Molecular dynamics with quantum transitions. J. Chem. Phys. 101, 4657–4667 (1994).
- J. F. Yang, X. M. Wen, H. Z. Xia, R. Sheng, Q. S. Ma, J. Kim, P. Tapping, T. Harada, T. W. Kee, F. Z. Huang, Y. B. Cheng, M. Green, A. Ho-Baillie, S. J. Huang, S. Shrestha, R. Patterson, G. Conibeer, Acoustic-optical phonon up-conversion and hot-phonon bottleneck in lead-halide perovskites. *Nat. Commun.* 8, 14120 (2017).
- O. Yaffe, Y. S. Guo, L. Z. Tan, D. A. Egger, T. Hull, C. C. Stoumpos, F. Zheng, T. F. Heinz, L. Kronik, M. G. Kanatzidis, J. S. Owen, A. M. Rappe, M. A. Pimenta, L. E. Brus, Local polar fluctuations in lead halide perovskite crystals. *Phys. Rev. Lett.* 118, 136001 (2017).

SCIENCE ADVANCES | RESEARCH ARTICLE

- E. Cinquanta, D. Meggiolaro, S. G. Motti, M. Gandini, M. J. P. Alcocer, Q. A. Akkerman, C. Vozzi, L. Manna, F. De Angelis, A. Petrozza, S. Stagira, Ultrafast THz probe of photoinduced polarons in lead-halide perovskites. *Phys. Rev. Lett.* 122, 166601 (2019).
- K. Miyata, D. Meggiolaro, M. T. Trinh, P. P. Joshi, E. Mosconi, S. C. Jones, F. De Angelis, X. Y. Zhu, Large polarons in lead halide perovskites. Sci. Adv. 3, e1701217 (2017).
- D. L. Anderson, O. L. Anderson, The bulk modulus-volume relationship for oxides. J. Geophys. Res. 75, 3494–3500 (1970).
- V. G. Baonza, General behavior of longitudinal optical phonons in cubic diatomic crystals. Solid State Commun. 130. 383–386 (2004).
- F. Aguado, V. G. Baonza, Prediction of bulk modulus at high temperatures from longitudinal phonon frequencies: Application to diamond, c-BN, and 3C-SiC. Phys. Rev. B 73, 024111 (2006).
- X.-Y. Zhu, V. Podzorov, Charge carriers in hybrid organic-inorganic lead halide perovskites might be protected as large polarons. J. Phys. Chem. Lett. 6, 4758–4761 (2015).
- 49. K. Miyata, X.-Y. Zhu, Ferroelectric large polarons. Nat. Mater. 17, 379–381 (2018).
- W. B. Chu, W. A. Saidi, Q. J. Zheng, Y. Xie, Z. G. Lan, O. V. Prezhdo, H. Petek, J. Zhao, Ultrafast dynamics of photongenerated holes at a CH₃OH/TiO₂ Rutile Interface. *J. Am. Chem.* Soc. 138, 13740–13749 (2016).
- Q. J. Zheng, W. A. Saidi, Y. Xie, Z. G. Lan, O. V. Prezhdo, H. Petek, J. Zhao, Phonon-assisted ultrafast charge transfer at van der Waals heterostructure interface. *Nano Lett.* 17, 6435–6442 (2017).
- G. Kresse, J. Hafner, Ab initio molecular dynamics for liquid metals. Phys. Rev. B 47, 558–561 (1993).
- G. Kresse, D. Joubert, From ultrasoft pseudopotentials to the projector augmented-wave method. *Phys. Rev. B* 59, 1758–1775 (1999).
- H. M. Jaeger, S. Fischer, O. V. Prezhdo, Decoherence-induced surface hopping. J. Chem. Phys. 137, 22A545 (2012).
- S. V. Kilina, A. J. Neukirch, B. F. Habenicht, D. S. Kilin, O. V. Prezhdo, Quantum zeno effect rationalizes the phonon bottleneck in semiconductor quantum dots. *Phys. Rev. Lett.* 110, 180404 (2013)
- J. P. Perdew, K. Burke, M. Ernzerhof, Generalized gradient approximation made simple. Phys. Rev. Lett. 77, 3865–3868 (1996).
- S. Grimme, J. Antony, S. Ehrlich, H. Krieg, A consistent and accurate ab initio parametrization of density functional dispersion correction (DFT-D) for the 94 elements H-Pu. J. Chem. Phys. 132, 154104 (2010).
- M. H. Du, Efficient carrier transport in halide perovskites: Theoretical perspectives.
 J. Mater. Chem. A 2, 9091–9098 (2014).
- P. Umari, E. Mosconi, F. De Angelis, Relativistic GW calculations on CH₃NH₃Pbl₃ and CH₃NH₃Snl₃ perovskites for solar cell applications. Sci. Rep. 4, 4467 (2014).
- A. V. Akimov, A simple phase correction makes a big difference in nonadiabatic molecular dynamics. J. Phys. Chem. Lett. 9, 6096–6102 (2018).
- Q. F. Dong, Y. J. Fang, Y. C. Shao, P. Mulligan, J. Qiu, L. Cao, J. S. Huang, Electron-hole diffusion lengths > 175 μm in solution-grown CH₃NH₃Pbl₃ single crystals. Science 347, 967–970 (2015).
- Y. Yang, M. J. Yang, Z. Li, R. Crisp, K. Zhu, M. C. Beard, Comparison of recombination dynamics in CH₃NH₃PbBr₃ and CH₃NH₃PbI₃ perovskite films: Influence of exciton binding energy. *J. Phys. Chem. Lett.* 6, 4688–4692 (2015).

- A. Alkauskas, A. Pasquarello, Band-edge problem in the theoretical determination of defect energy levels: The O vacancy in ZnO as a benchmark case. *Phys. Rev. B* 84, 125206 (2011)
- W. M. Chen, B. Monemar, E. Janzén, J. L. Lindström, DIRECT observation of intercenter charge-transfer in dominant nonradiative recombination channels in silicon. *Phys. Rev. Lett.* 67, 1914–1917 (1991).
- D. Macdonald, A. Cuevas, Validity of simplified Shockley-Read-Hall statistics for modeling carrier lifetimes in crystalline silicon. *Phys. Rev. B* 67, 075203 (2003).
- S. Rein, S. W. Glunz, Electronic properties of the metastable defect in boron-doped Czochralski silicon: Unambiguous determination by advanced lifetime spectroscopy. Appl. Phys. Lett. 82, 1054–1056 (2003).
- D. Macdonald, L. J. Geerligs, Recombination activity of interstitial iron and other transition metal point defects in p- and n-type crystalline silicon. Appl. Phys. Lett. 85, 4061–4063 (2004).
- C. Wehrenfennig, G. E. Eperon, M. B. Johnston, H. J. Snaith, L. M. Herz, High charge carrier mobilities and lifetimes in organolead trihalide perovskites. *Adv. Mater.* 26, 1584–1589
- S. K. Estreicher, T. M. Gibbons, B. Kang, M. B. Bebek, Phonons and defects in semiconductors and nanostructures: Phonon trapping, phonon scattering, and heat flow at heterojunctions. *J. Appl. Phys.* 115, 012012 (2014).

Acknowledgments: We thank A. V. Akimov and X. Zhang for fruitful discussions and H. Chen for carefully reading the manuscript, Funding: W.A.S. acknowledges a start-up fund from the Department of Mechanical Engineering and Materials Science at the University of Pittsburgh and partial funding from NSF (award no. DMR-1809085), J.Z. acknowledges the support of the National Natural Science Foundation of China (grant nos. 11620101003 and 11704363) and the National Key R&D Program of China (grant nos. 2016YFA0200604 and 2017YFA0204904), O.V.P. acknowledges funding from the U.S. Department of Energy (DOE) (grant no. DE-SC0014429). Calculations were performed, in part, at the Environmental Molecular Sciences Laboratory at the PNNL, a user facility sponsored by the DOE Office of Biological and Environmental Research, Supercomputing Center at USTC, the University of Pittsburgh Center for Research Computing (CRC) through the computational resources, and Argonne Leadership Computing Facility, which is a DOE Office of Science User Facility supported under contract DE-AC02-06CH11357. Author contributions: W.C. carried out calculations with the help of Q.Z. J.Z. and W.A.S. supervised the studies and the writing of the manuscript. All authors discussed the results. Competing interests: The authors declare that they have no competing interests. Data and materials availability: All data needed to evaluate the conclusions in the paper are present in the paper and/or the Supplementary Materials. Additional data related to this paper may be requested from the authors.

Submitted 21 January 2019 Accepted 25 November 2019 Published 14 February 2020 10.1126/sciadv.aaw7453

Citation: W. Chu, Q. Zheng, O. V. Prezhdo, J. Zhao, W. A. Saidi, Low-frequency lattice phonons in halide perovskites explain high defect tolerance toward electron-hole recombination. *Sci. Adv.* **6**, eaaw7453 (2020).



Low-frequency lattice phonons in halide perovskites explain high defect tolerance toward electron-hole recombination

Weibin Chu, Qijing Zheng, Oleg V. Prezhdo, Jin Zhao and Wissam A. Saidi

Sci Adv **6** (7), eaaw7453. DOI: 10.1126/sciadv.aaw7453

ARTICLE TOOLS http://advances.sciencemag.org/content/6/7/eaaw7453

SUPPLEMENTARY http://advances.sciencemag.org/content/suppl/2020/02/10/6.7.eaaw7453.DC1 MATERIALS

REFERENCES This article cites 69 articles, 5 of which you can access for free

http://advances.sciencemag.org/content/6/7/eaaw7453#BIBL

PERMISSIONS http://www.sciencemag.org/help/reprints-and-permissions

Use of this article is subject to the Terms of Service